Research Article

optica

Chip-to-chip quantum photonic interconnect by path-polarization interconversion

JIANWEI WANG[1], DAMIEN BONNEAU[1], MATTEO VILLA[1, 2], JOSHUA W. SILVERSTONE[1], RAFFAELE SANTAGATI[1], SHIGEHITO MIKI[3], TARO YAMASHITA[3], MIKIO FUJIWARA[4], MASAHIDE SASAKI[4], HIROTAKA TERAI[3], MICHAEL G. TANNER[5], CHANDRA M. NATARAJAN[5], ROBERT H. HADFIELD[5], JEREMY L. O'BRIEN[1], AND MARK G. THOMPSON[1, *]

[1] *Centre for Quantum Photonics, H. H. Wills Physics Laboratory & Department of Electrical and Electronic Engineering, University of Bristol, Merchant Venturers Building, Woodland Road, Bristol BS8 1UB, United Kingdom.*
[2] *Istituto di Fotonica e Nanotecnologie (IFN), Dipart di Fisica-Politecnico di Milano, Piazza Leonardo da Vinci 32, 20133 Milano–Italia.*
[3] *National Institute of Information and Communications Technology (NICT), 588-2 Iwaoka, Kobe 651-2492, Japan.*
[4] *National Institute of Information and Communications Technology (NICT), 4-2-1 Nukui-Kitamachi, Koganei, Tokyo 184-8795, Japan.*
[5] *School of Engineering, University of Glasgow, G12 8QQ, United Kingdom.*
**Corresponding author: mark.thompson@bristol.ac.uk*

Received XX Month XXXX; revised XX Month, XXXX; accepted XX Month XXXX; posted XX Month XXXX (Doc. ID XXXXX); published XX Month XXXX

Integrated photonics has enabled much progress towards quantum technologies. Many applications, e.g., quantum communication, sensing, and distributed cloud quantum computing, require coherent photonic interconnection between separate on-chip subsystems. Large-scale quantum computing architectures and systems may ultimately require quantum interconnects to enable scaling beyond the limits of a single wafer, and towards multi-chip systems. However, coherently connecting separate chips remains a challenge, due to the fragility of entangled quantum states. The distribution and manipulation of entanglement between multiple integrated devices is one of the strictest requirements of these systems. Here, we report the first quantum photonic interconnect, demonstrating high-fidelity entanglement distribution and manipulation between two separate photonic chips, implemented using state-of-the-art silicon photonics. Path-entangled states are generated on one chip, and distributed to another chip by interconverting between path and polarization degrees of freedom, via a two-dimensional grating coupler on each chip. This path-to-polarization conversion allows entangled quantum states to be coherently distributed. We use integrated state analyzers to confirm a Bell-type violation of S=2.638±0.039 between the two chips. With further improvements in loss, this quantum photonic interconnect will provide new levels of flexibility in quantum systems and architectures. © 2014 Optical Society of America

OCIS codes: *(270.0270) Quantum optics; (270.5565), (270.5585) Quantum information and processing; (130.0130) Integrated optics.*

http://dx.doi.org/10.1364/optica.99.099999

1. Introduction

Further progress towards quantum communication [1, 2], sensing [3] and computing [4, 5] will greatly benefit from a "quantum photonic interconnect" (henceforth QPI): an inter-/intra-chip link—e.g. in optical fiber or free-space—capable of coherently distributing quantum information and entanglement between on-chip sub-systems within a single complete quantum system. The significance of quantum interconnectivity was first highlighted by Kimble [1]. Here we study a chip-based interconnect solution, which will be essential in many future applications and provide substantial architectural flexibility. Secure quantum key distribution and quantum communications [6–8], and distributed and even cloud quantum computing [9–11], for example, will require interconnected on-chip subsystems in practice. Precise quantum sensing will gain more flexibility and versatility from on-chip generation and measurement of entanglement, with the interaction with the sample occurring remotely, in a different medium or location (e.g. chip, fiber, and free-space [12–14]). Quantum computing will greatly benefit from this QPI through architectural simplifications [15–17]; easier integration of materials, and platforms optimized for the performance of source [18–19], circuit [20–28], detector [29–30], and such as optical delays and memories. Ultimately, large-scale integrated quantum systems and devices may even exceed the area of a single wafer or require interconnects for architectural reasons.

A QPI must coherently and robustly transmit a qubit state $\alpha|0\rangle+\beta|1\rangle$ between subsystems [1], in which the relative phase information must be maintained, as in classical coherent optical communication protocols [33]. The quantum photonic interconnect must be capable of coherently interconverting between the preferred encodings in the platforms and media through which it connects [1, 34]. Perhaps, the most demanding requirement for a quantum interconnect is the preservation of high-fidelity qubit entanglement throughout manipulation, conversion, and transmission processes within the full chip-based system. Path-encoding [20–25] in two waveguides is the most common and natural choice for the encoding of qubits on-chip. However, encoding qubits in two separate free-space or fiber links needs sub-wavepacket path-length matching, and fast active phase stabilization. Polarization [6–10], spatial-mode [35, 36], or time-bin [37] encoding is typical for off-chip qubit transmission and distribution. For example, the state of polarization is robust in free-space, and in optical fiber (birefringence-induced fluctuation can be actively corrected on slow time scales [38]). Already there have been demonstrations of many important features of

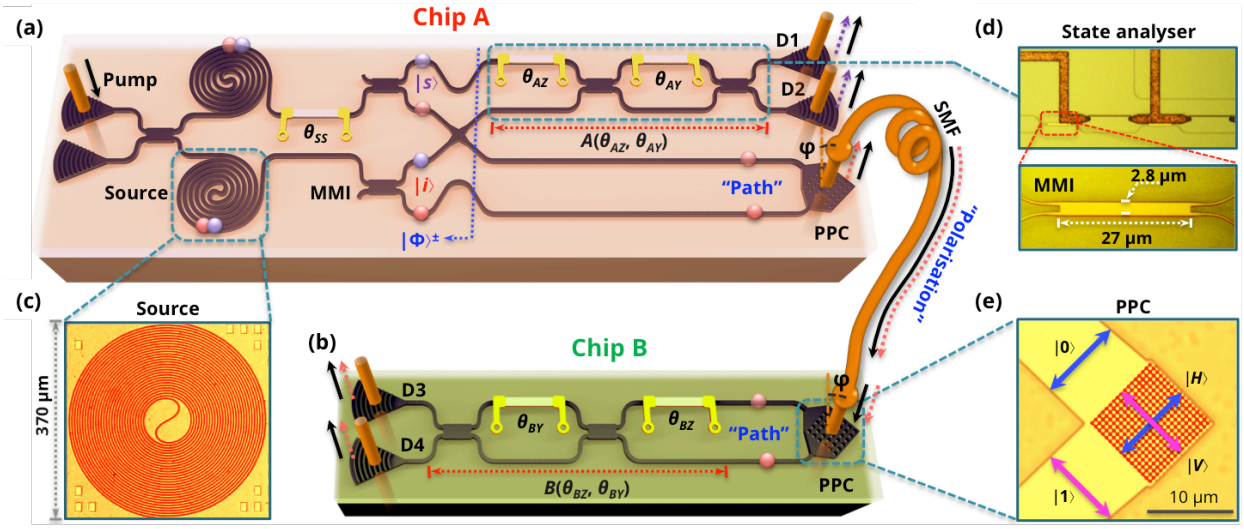

Fig. 1. Quantum photonic interconnect and entanglement distribution between two integrated silicon photonic chips. (a) Chip-A comprises three stages, path-entangled states generation, arbitrary projective measurement $A(\theta_{AZ}, \theta_{AY})$, and path–polarization interconversion (PPC). (b) Chip-B includes projective measurement $B(\theta_{BZ}, \theta_{BY})$ and PPC stages. On the chip-A, signal-idler photon-pairs are created in the spiraled waveguide single-photon source. Bell states $|\Phi\rangle^{\pm}$ are then produced when θ_{SS} is controlled to be $\pi/2$ or π. Idler qubit initially encoded in path are coherently coupled to polarization-encoding and transmitted through a 10 meter single-mode optical fiber (SMF), and reversely converted back to path-encoding on the chip-B. Signal qubit is analyzed using $A(\theta_{AZ}, \theta_{AY})$ on chip-A and idler qubit is analyzed using $B(\theta_{BZ}, \theta_{BY})$ on chip-B. The 2D grating coupler, behaving as the path–polarization converter (PPC), is used to coherently interconvert photonic qubits between path-encoding on chip and polarization-encoding in fiber. Optical microscopy images of, (c) the photon-pair source, (d) the arbitrary state analyzer (inset shows the MMI splitter), and (e) the 2D grating coupler PPC structure.

generation and manipulation [20–26, 39, 40], photon detection [29, 30], interfacing of different degrees of freedom [41–43], and multi-chip links [31, 32]. However, to date there has been no demonstration of a full QPI system capable of distributing qubit entanglement across two or more integrated quantum photonic devices.

Here, we demonstrate a high-fidelity QPI. Telecom-band entangled photons are generated, manipulated and distributed between two integrated silicon photonic chips linked by a single mode optical fiber. These devices and chips were fabricated using state-of-the-art silicon photonics to enable and monolithically integrate all key capabilities required to demonstrate the quantum interconnect. Maximally path-entangled qubit states are generated and manipulated on-chip. These states are distributed across two silicon chips, by transmitting one qubit from one chip to the other via a fiber link. To preserve coherence across two chips, we used two-dimensional grating coupler devices [40, 41] to interconvert between path (on-chip) and polarization (in fiber) degrees of freedom. We demonstrate this process with high fidelity. Each qubit is analyzed in its respective chip using thermal phase shifters to form arbitrary integrated state analyzers. We implement a rigorous test of entanglement—confirming a strong Bell-type inequality violation of 16.4σ and 15.3σ. Together with further improvements in loss, this approach will facilitate new quantum technologies and applications that rely on, or benefit from QPIs.

2. Experiment

A. Experimental setup

Our chip-to-chip QPI system is shown schematically in Figs. 1(a) and (b). This system generates path-entangled states on chip-A and coherently distributes one entangled qubit to chip-B, via an optical fiber link.

A filtered 50-mW continuous-wave pump (λ_p=1555.5 nm) is coupled into chip-A and split into two paths using a multimode interference coupler (MMI) with a ~50/50 splitting ratio [44] (Fig. 1(d)). Each path is connected to a photon-pair source. One photon pair is produced in superposition between these two sources, which, after post-selection on measuring a coincidence, yields the photon-number entangled state $(|1_s1_i\rangle|0_s0_i\rangle - e^{i2\theta_{SS}}|0_s0_i\rangle|1_s1_i\rangle)/\sqrt{2}$, where θ_{SS} is the phase after the two sources [22]. Each source produces signal-idler photon pairs (λ_s=1550.7 nm, λ_i=1560.3 nm) via spontaneous four-wave mixing (SFWM, [19]) inside a 20-mm-long spiraled waveguide (Fig. 1(c)). Signal and idler photons are probabilistically separated by two demultiplexing MMI couplers, and post-selected by two off-chip spectral filters (with a 25% success probability; see Supplement). These modes are then swapped using a waveguide crossing to yield a path-entangled qubit-basis Bell state $|\Phi\rangle^{\pm} = (|00\rangle \pm |11\rangle)/\sqrt{2}$ (when θ_{SS} equals to $(n + 1/2)\pi$ or $n\pi$ for an integer n, with the subscripts referring to signal or idler photons).

The signal qubit is manipulated and measured on the same chip (chip-A) by an single qubit measurement stage $A(\theta_{AZ}, \theta_{AY})$. This consists of a thermo-optically driven Mach-Zehnder interferometer with an additional thermal phase shifter (Fig. 1(d)). The path-encoded idler qubit is directed to an on-chip path-to-polarization converter (PPC). This device, described in more detail in the next section, coherently interconverts the qubit from an on-chip path encoding to an in-fiber polarization encoding. After transmission across the fiber link, chip-B reverses this process, converting the polarization-encoded qubit back to on-chip path encoding, via a second PPC. There, it is measured by a second single qubit measurement stage $B(\theta_{BZ}, \theta_{BY})$ (Fig. 1(b)). In our experiment, the QPI consists of the fiber link bracketed by these two PPCs.

The polarization in the fiber can drift over time due to changes in environmental conditions (stress, vibrations, temperature, etc). Due to the relatively short length of fiber used in this experiment (10 m), the fiber link was used without any control of its environment, other than to fix it to our optical table. Longer links may need active phase (i.e. polarization) compensation and control [38].

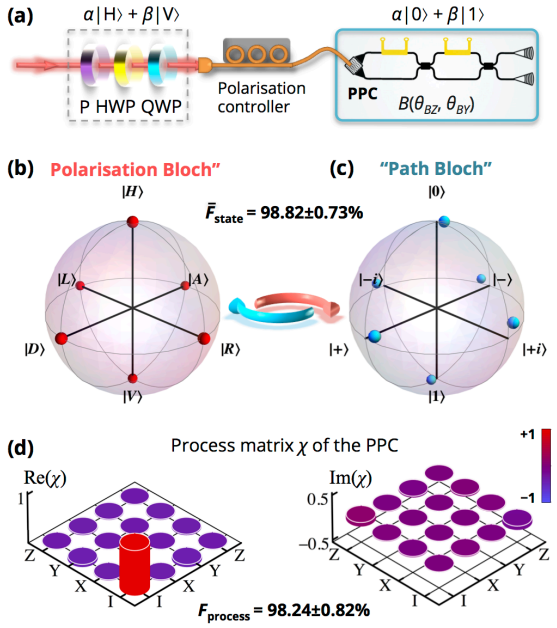

Fig. 2. Interconversion of polarization-encoding and path-encoding. (a) Initial arbitrary polarization-encoded states $\alpha|H\rangle+\beta|V\rangle$ ($|H\rangle$ and $|V\rangle$ are two orthogonally polarized states) were prepared by using a set of bulk optic polarizer (P), half-wave plate (HWP), and quarter-wave plate (QWP). A fiber-based polarization controller was used to compensate polarization rotation in the single mode fiber. The PPC interconverted the polarization-encoded states into on-chip path-encoded states $\alpha|0\rangle+\beta|1\rangle$, where $|0\rangle$ and $|1\rangle$ denote path states in two waveguides. The path-encoded states were then analyzed using the integrated analyzer $B(\theta_{BZ}, \theta_{BY})$ to implement state tomography. The Bloch sphere representation of, (b) ideal polarization-encoded states $|H\rangle$, $|V\rangle$, $|D\rangle$, $|A\rangle$, $|R\rangle$, and $|L\rangle$ in bulk optics (red points), and (c) measured path-encoded states $|0\rangle$, $|1\rangle$, $|+\rangle$, $|-\rangle$, $|+i\rangle$, and $|-i\rangle$ on chip (blue points). The density matrix presentation of all these states is provided in Supplement. Indicated fidelity represents the mean over the six measured states. (d) Reconstructed process matrix χ of the PPC using the quantum process tomography.

After configuring the measurements on the two chips, photon pairs were detected by two fiber-coupled superconducting nanowire single photon detectors (SNSPDs) with ~50% efficiency and ~800 Hz dark counts [45], after passing through relatively narrow 1.2-nm spectral band-pass filters. Finally, photon coincident counts were recorded using a time interval analyzer. At the output of chip-A, ~500 photon pairs per second were measured, dropping to ~12 pairs per second after the idler photon had additionally traversed the QPI and chip-B. Ultimately, signal and idler photons had experienced 18 dB and 34 dB total attenuation, respectively.

B. Path-polarization interconversion

The PPC converts the two orthogonal polarization modes of the fiber into the fundamental transverse-electric (TE) modes of two on-chip waveguides. The stronger confinement of the TE mode in our silicon waveguide geometry (500nm×220nm) facilitates more efficient nonlinear optical photon-pair sources [39], and a higher integration density. Accordingly, we designed the PPC to couple into the TE mode of the silicon waveguide.

Our PPC is implemented using a 2D grating coupler (see Fig.1(e)), essentially formed by superposing two 1D grating couplers at right angles [40, 41]. In this way, the polarization state of the SMF fiber-transmitted photon is determined by the two-waveguide on-chip state, and vice versa, achieving path-polarization interconversion. Further

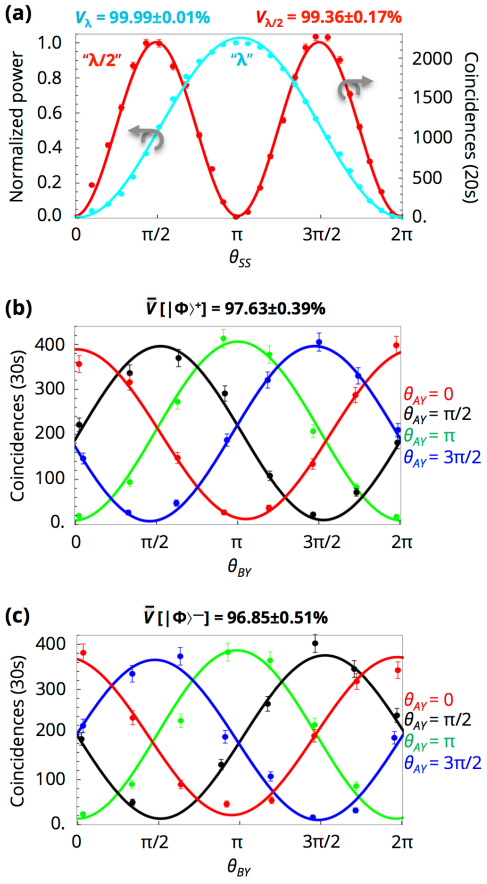

Fig. 3. Entanglement fringes. (a) "λ"-classical interference (cyan) and "$\lambda/2$"-quantum interference (red) fringes measured on the chip-A. Bright light was measured (normalized) at port D1, and coincidences were collected (accumulated 20s) between ports D1 and D2. The θ_{SS} was rotated to produce the fringes, when $A(\theta_{AZ}, \theta_{AY})$ was set as the *Hadamard* gate. Photons are bunched or anti-bunched when θ_{SS} is $n\pi$ and $(n+1/2)\pi$. (b) and (c) Entanglement correlation fringes for the Bell states $|\Phi\rangle^+$ and $|\Phi\rangle^-$ after distributed across the two chips. Coincidences were collected (accumulated 30s) between ports D1 and D3. The θ_{BY} on chip-B was continually rotated ($\theta_{BZ}=0$) to obtain the fringes, as $A(\theta_{AZ}, \theta_{AY})$ on chip-A was projected onto $\{|1\rangle, |0\rangle, |-\rangle, |+\rangle\}$ basis by setting the θ_{AY} to $\{0, \pi/2, \pi, 3\pi/2\}$ and θ_{AZ} to 0. The indicated visibility represents the mean over all four fringes. Error bars are given by Poissonian statistics, and accidental coincidences are subtracted.

To verify the PPC coherent mapping, we prepared arbitrary bright-light polarization states using bulk optical components and coupled them into the on-chip receiver (see Fig. 2(a)). The PPC allowed us to convert the polarization states into path-encoded states, which we analyzed on-chip performing quantum state tomography [34, 46]. We prepared a set of six polarization states ρ_{pol} in bulk optics, and measured the corresponding on-chip path states ρ_{path}; these states are respectively shown as Bloch (or Poincare) vectors in Figs. 2(b) and (c). We provide the full density matrix data of these states in the Supplement; these data correspond directly with the plotted Bloch vectors. The overlap between the input states and measured states can be described by the state fidelity, which is defined as $F_{state}=(Tr[(\rho_{pol}^{1/2}\rho_{path}\rho_{pol}^{1/2})^{1/2}])^2$. We find a mean state fidelity of the six states of 98.82±0.73%.

We also fully quantify the PPC process using a quantum process tomography [34]. This can be mathematically described by a process matrix χ, defined by $\rho_{path}=\sum_{mn}(E_m\rho_{pol}E_n^{\dagger}\chi_{mn})$, where E_i are the identity I and Pauli matrices X, Y, and Z, respectively. By injecting the ρ_{pol} states into the PPC and measuring the ρ_{path} states, we estimated the process

98.24±0.82%, defined as $F_{process} = Tr[\chi_{ideal}\,\chi]$, where χ_{ideal} is the ideal process matrix with unit *(I, I)* component. *X*, *Y*, and *Z* amplitudes of the matrix χ represent the probabilities of a bit-flip or phase-flip error in the PPC interconversion. The process fidelity is directly related to the device cross-talk, which we estimate as 18dB (98.4%). PPC designs with improved cross-talk (and loss) have been demonstrated [47, 48].

C. Entanglement correlation fringes

Our first observation of entanglement distribution between the two chips took the form of nonlocal fringes. We configured the chip-A to produce entangled photons. These photons were collected at ports D1 and D2 and routed to the detectors. Through a continual scanning of θ_{SS}, we observed "λ" (classical) and "$\lambda/2$" (quantum) interference fringes with a high visibility (defined as $V = 1-N_{min}/N_{max}$) of 99.99±0.01% and 99.36±0.17%, respectively (Fig. 3(a)). The high visibility of this phase-doubled fringe is a clear signature of the high-quality photon-number entanglement produced inside the chip-A [22,12]. These high visibilities arise from well-balanced MMI couplers [44] and from a good spectral overlap between the two sources within the narrow bandwidth of the signal and idler filters. The photon-number entangled state evolves into the path-entangled Bell states $|\Phi\rangle^+$ or $|\Phi\rangle^-$, depending on the setting of θ_{SS} (as described previously).

The entangled-qubits were then separated and distributed, with the signal qubit kept on chip-A and the idler sent via the QPI to chip-B. We measured correlation fringes across the two chips by continuously varying θ_{BY}, and setting θ_{AY} variously at 0, $\pi/2$, π, and $3\pi/2$, while collecting coincidences between ports D1 and D3. Fig. 3(b) and Fig. 3(c) respectively show these fringes for the two Bell states $|\Phi\rangle^+$ and $|\Phi\rangle^-$. These experimental results are in good agreement with the theoretical model $\cos^2[(\theta_{AY}\pm\theta_{BY})/2]$ [49], with a small phase offset due to device calibration. These fringes exhibit a mean visibility of 97.63±0.39% and 96.85±0.51%, respectively, above the quantum threshold of $1/\sqrt{2}$ (71%) required to violate the Bell inequality [50]. These data show that entanglement is produced on chip-A and faithfully transferred to chip-B.

D. Bell-CHSH measurement

A strict test of the existence and level of entanglement distributed between the two chips is the Bell-CHSH test (Clauser-Horne-Shimony-Holt) [51, 52]. The CHSH inequality is defined as:

$$S = |\langle A_1, B_1\rangle + \langle A_1, B_2\rangle + \langle A_2, B_1\rangle - \langle A_2, B_2\rangle| \leqslant 2 \qquad (1)$$

where A_i and B_i briefly denote the projectors $A(0, \theta_{AY})$ and $B(0, \theta_{BY})$ on two chips. Normalized correlation coefficients $\langle A_i, B_i\rangle$ were measured when θ_{AY} on the chip-A was chosen to be $\{0, \pi/2\}$ and θ_{BY} on the chip-B was simultaneously chosen to be $\{\pi/4, 3\pi/4\}$. Full data of $\langle A_i, B_i\rangle$ is provided in Table 1. Substituting them into equation (1), we obtained the directly measured S_{CHSH} values of 2.638±0.039 and 2.628±0.041 for the two Bell states $|\Phi\rangle^+$ and $|\Phi\rangle^-$, respectively. These S_{CHSH} parameters violate the Bell-CHSH inequality by 16.4 and 15.3 standard deviations, respectively, strongly confirming that the two photons after distribution are highly entangled. Moreover, we also estimate the maximally achievable S_{fringe} value of 2.761±0.011 and 2.739±0.015 for the $|\Phi\rangle^+$ or $|\Phi\rangle^-$ states, from the mean visibility of the entanglement correlation fringes (Fig. 3(b) and Fig. 3(c)) according to $S_{fringe} = 2\sqrt{2} \times V$ [50]. Fig. 4 illustrates the good agreement between S_{CHSH} and S_{fringe}, confirming the high-performance of the chip-to-chip QPI.

Several possible explanations exist for the small discrepancy between the S_{fringe} and S_{CHSH} values. Firstly, S_{fringe} strictly provides an upper bound on S_{CHSH}, which is saturated only when the Bell-CHSH measurement projectors align with the state in question, and when the detection efficiencies are the same for all measurements [53]. Miscalibration of the measurement projectors, or fluctuations in the fibre-chip coupling (see Supplementary Fig. S4) could both reduce S_{CHSH}.

Table 1. Measured Bell-CHSH correlation coefficients.

$(\theta_{AY}, \theta_{BY})$	$\|\Phi\rangle^+$ $\langle A_i, B_i\rangle$	$\|\Phi\rangle^-$ $\langle A_i, B_i\rangle$
$(0, \pi/4)$	0.601±0.021	0.673±0.021
$(0, 3\pi/4)$	-0.692±0.018	-0.589±0.023
$(\pi/2, \pi/4)$	0.692±0.019	-0.652±0.020

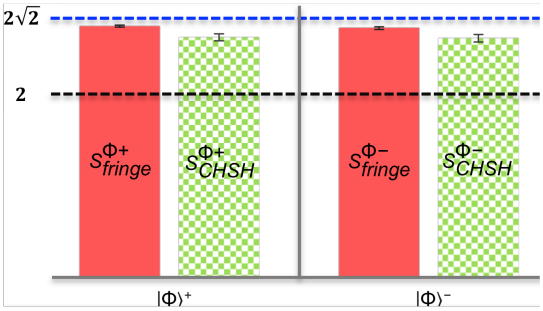

Fig. 4. Verification of chip-to-chip entanglement distribution and quantum photonic interconnect. The two Bell entangled-states $|\Phi\rangle^{\pm}$ were distributed across the two silicon chips. The *S* parameters were obtained using two methods. Green dotted columns are the directly measured S_{CHSH} by substituting correlation coefficients (Table 1) into Eq. (1). Pink columns are the maximal achievable S_{fringe}, estimated from the mean visibility of correlation fringes in Fig.3. The S_{CHSH} and S_{fringe} parameters are in good agreement. Black and blue dashed lines denote the classical and quantum boundary. These results confirm the high level of entanglement after distributed across the two chips, and the high quality of the quantum photonic interconnect. Each coincidences measurement was accumulated for 60*s*. Accidental coincidences are subtracted, and error bars (±1 s. d.) are given by Poissonian statistics.

3. Conclusion

We have now demonstrated high-fidelity entanglement generation, manipulation, interconversion, distribution, and measurement across two separate integrated photonic devices, achieving the first chip-to-chip quantum photonic interconnect. The use of path–polarization interconversion preserves coherence across the fully interconnected chip-fiber-chip system.

Our system could be improved in several ways. The efficiency and fidelity [47, 48] of this interconversion process can be improved, and other off-chip encodings (e.g. orbital angular momentum [54, 55] or time bin [56]) may further enrich this quantum interconnectivity. The spiral photon-pair sources used here require no tuning to achieve spectral overlap, whereas optical microring resonators facilitate higher photon flux, produce spectrally uncorrelated photons [23, 57], and have a smaller footprint, but require careful tuning. Finally, the coupling fluctuations we observed could be avoided by optically packaging the chip, enabling a more robust and portable chip-to-chip quantum system.

A robust QPI will facilitate new applications of quantum technology. This chip-to-chip quantum interconnectivity could be used for short-distance secret key sharing between bank and user, for example. Remote quantum sensing could be made possible by this system, allowing the quantum metrology of remote, possibly birefringent, analytes. Chip-to-chip interconnectivity would bring architectural flexibility to the design of linear optical quantum computers, potentially allowing quantum computation to be distributed over chip-based subsystems. In addition, the use of silicon technology allows large-scale integration [28, 58, 59] and compatibility with microelectronics and telecommunications infrastructure [60], and offers ability to monolithically integrate photon sources [19, 23], circuits [22, 28], and detectors [29, 30]. Our work opens the door to multi-chip integrated quantum photonic systems, capable of robustly distributing and transmitting quantum information among chips.

Appendix A: Devices design and fabrication.

Chip-A and chip-B respectively have a device footprint of 1.2×0.5 mm^2 and 0.3×0.05 mm^2. These devices were fabricated on the standard silicon-on-insulator wafer with a 220 *nm* silicon layer and a 2 μm buried silica oxide layer. The MMI couplers were designed as 2.8 μm × 27 μm to get a nearly balanced splitting ratio (Fig.1(d)). MMIs can offer a large bandwidth and large fabrication tolerance. We used the same MMIs design as Ref [22] and we both observed high-visibility classical and quantum interference, reflecting its excellent reproducibility. Spiraled waveguide sources with a 2 *cm* length were used to create photon-pairs. The 1D grating couplers consist of a periodic 315 *nm* silicon layer with a 630 *nm* pitch. The 2D grating couplers include 10 μm × 10 μm hole arrays with a 390 *nm* diameter and 605 *nm* pitch. Resistive heaters with a 50 μm length were designed and formed by a Ti/TiN metal layer. The devices were fabricated using the deep-UV (193 *nm*) lithography at LETI-ePIXfab. Silicon waveguides were 220 *nm* fully etched, while grating couplers were 70 *nm* shallow etched. The devices were covered by a 1.6 μm silica oxide layer.

Appendix B: Devices characterizations.

Optical accesses and electric accesses were independently controlled on two chips (Supplementary Fig. S1). Optical access was achieved using *V*-groove single modes fiber arrays with a 127 μm pitch. Fibers were titled with an angle of φ= 10~12 degrees to guarantee grating couplers work at the required wavelengths (Fig1). The waveguide crosser had a cross-talk of about -40 dB. The extinction ratio of the MZI structures was measured to be more than 30 dB, corresponding to MMIs with a 50%±1% reflectivity. The polarization extinction ratio of 1D and 2D grating couplers was measured to be larger than 20 dB and 18 dB, respectively. Excess loss of 1D and 2D grating couplers were about -4.8 dB and -7.6 dB at peak wavelengths, respectively (see Supplementary Fig.S2). We made estimation of losses from different contributors in the full system: -6 dB from off-chip filters, -6 dB from SSNPDs, -9.5 dB from 1D grating couplers, -15.2 dB from 2D grating couplers, -6 dB from demultiplexing MMIs, and -8 dB from MMIs loss and propagation loss in waveguide. Totally, signal and idler photons respectively experienced -18 dB and -34 dB attenuation. We tested several copies of the devices and they all exhibited similar performance.

All thermal-driven phase shifters were controlled using homemade electronic controllers. Wire bounding technology was used to contact heaters' transmission lines. Optical power was recorded as a function of electric power added on heaters. The optical—electric power contour was fitted and used to construct the mapping between the required states and electric power. Supplementary Fig.S3 shows the calibration results of chip-A's and chip-B's state analyzers. To avoid the influence of temperature variation, both two chips were mounted on temperature-stabilized stages. The pump light propagates collinearly with single photons, and we use this bright light to perform fiber realignment using piezo-electronic stacks, and to monitor that photon states are stable in time throughout the full system. Supplementary Fig.S4 shows the stability of the chip-to-chip system, which indicates path-encoded states on the two chips and polarization-encoded states in the fiber are both stable in time.

Funding sources and acknowledgments. This work was supported by the Engineering and Physical Science Research Council (EPSRC, UK), the European Research Council, the Bristol Centre for Nanoscience and Quantum Information, the European FP7 project BBOI, UK Quantum Communications Hub project, and the ImPACT Program of the Cabinet Office Japan. J.L.O'B. acknowledges a Royal Society Wolfson Merit Award and a Royal Academy of Engineering Chair in Emerging Technologies. M.G.Th. acknowledges support from an EPSRC Early Career Fellowship.

Acknowledgment. We thank G. D. Marshall and W. A. Murray for experiment assistance and C. Erven, T. Rudolph, A. Laing, P. J. Shadbolt, J. C. F. Matthews, P. Turner, L. Kling, D. Dai, Y. Ding, and X. Cai for useful discussions.

See Supplement 1 for supporting content.

REFERENCES

1. H. J. Kimble, The quantum internet. Nature 453, 1023–1030 (2008).
2. N. Gisin, R. Thew, Quantum communication. Nat. Photon. 1, 165–171 (2007).
3. V. Giovannetti, S. Lloyd, L. Maccone, Advances in quantum metrology. Nat. Photon. 5, 222–229 (2011).
4. T. D. Ladd, F. Jelezko, R. Laflamme, Y. Nakamura, C. Monroe, J. L. O'Brien, Quantum computers. Nature 464, 45–53 (2010).
5. J. L O'Brien, Optical Quantum Computing. Science 318, 1567–1570 (2007).
6. J. Yin, J. G. Ren, H. Lu, Y. Cao, H. L. Yong, Y.-P. Wu, C. Liu, S. K. Liao, F. Zhou, Y. Jiang, X. D. Cai, P. Xu, G. S. Pan, J. J. Jia, Y. M. Huang, H. Yin, J. Y. Wang, Y. A. Chen, C. Z. Peng, J. W. Pan, Quantum teleportation and entanglement distribution over 100-kilometre free-space channels. Nature 488, 85–188 (2012).
7. X. S. Ma, T. Herbst, T. Scheidl, D. Wang, S. Kropatschek, W. Naylor, B. Wittmann, A. Mech, J. Kofler, E. Anisimova, V. Makarov, T. Jennewein, R. Ursin, A. Zeilinger, Quantum teleportation over 143 kilometres using active feedforward. Nature 489, 269–273 (2012).
8. R. Ursin, T. Jennewein, M. Aspelmeyer, R. Kaltenbaek, M. Lindenthal, P. Walther, A. Zeilinger, Quantum teleportation across the Danube. Nature 430, 849–849 (2004).
9. S. Barz, E. Kashefi, A. Broadbent, J. F. Fitzsimons, A. Zeilinger, P. Walther, Demonstration of Blind Quantum Computing. Science 335, 303–308 (2012).
10. K. A. G. Fisher, A. Broadbent, L. K. Shalm, Z. Yan, J. Lavoie, R. Prevedel, T. Jennewein, K. J. Resch, Quantum computing on encrypted data. Nat. Commun. 5 (2014).
11. J. I. Cirac, A. K. Ekert, S. F. Huelga, C. Macchiavello, Distributed quantum computation over noisy channels. Phys. Rev. A 59, 4249–4254 (1999).
12. J. C. F. Matthews, A. Politi, StefanovAndre, J. L. O'Brien, Manipulation of multiphoton entanglement in waveguide quantum circuits. Nat. Photon. 3, 346–350 (2009).
13. A. Crespi, M. Lobino, J. C. F. Matthews, A. Politi, C. R. Neal, R. Ramponi, R. Osellame, J. L. O'Brien, Measuring protein concentration with entangled photons. Appl. Phys. Lett. 100, 233704 (2012).
14. T. Nagata, R. Okamoto, J. L. O'Brien, K. Sasaki, S. Takeuchi, Beating the Standard quantum limit with four-entangled photons, Science 316, 726-729, 2007.
15. N. H. Nickerson, J. F. Fitzsimons, S. C. Benjamin, Freely scalable quantum technologies using cells of 5-to-50 qubits with very lossy and noisy photonic links. Phys. Rev. X 4, 041041 (2014).
16. K. Kieling, T. Rudolph, and J. Eisert, Percolation, Renormalization, and Quantum Computing with Nondeterministic Gates. Phys. Rev. Lett. 99, 130501 (2007).
17. M. G. Segovia, P. Shadbolt, D. E. Browne, T. Rudolph, From three-photon Greenberger-Horne-Zeilinger states to ballistic universal quantum computation. Phys. Rev. Lett. 115, 020502 (2015).
18. R. Horn, P. Abolghasem, B. J. Bijlani, D. Kang, A. S. Helmy, G.Weihs, Monolithic source of photon pairs. Phys. Rev. Lett. 108, 153605 (2012).
19. S. Clemmen, K. P. Huy, W. Bogaerts, R. G. Baets, P. Emplit, S. Massar, Continuous wave photon pair generation in silicon-on-insulator waveguides and ring resonators. Opt. Express 17, 16558–16570 (2009).
20. A. Politi, M. J. Cryan, J. G. Rarity, S. Yu, J. L. O'Brien, Silica-on-Silicon waveguide quantum circuits. Science 320, 646–649 (2008).
21. P. J. Shadbolt, M. R. Verde, A. Peruzzo, A. Politi, A. Laing, M. Lobino, J. C. F. Matthews, M. G. Thompson, J. L. O'Brien, Generating, manipulating and measuring entanglement and mixture with a reconfigurable photonic circuit. Nat. Photon. 6, 45–49 (2012).
22. J. W. Silverstone, D. Bonneau, K. Ohira, N. Suzuki, H. Yoshida, N. Iizuka, M. Ezaki, C. M. Natarajan, M. G. Tanner, R. H. Hadfield, V. Zwiller, G. D. Marshall, J. G. Rarity, J. L. O'Brien, M. G. Thompson. On-chip quantum interference between silicon photon-pair sources. Nat. Photon. 8, 104–108

23. J. W. Silverstone, D. Bonneau, M. Strain, M. Sorel, J. L. O'Brien, M. G. Thompson. Qubit entanglement between ring resonator photon-pair sources on a silicon chip. Nat. Commun. 6, 7948 (2015).
24. S. Tanzilli, A. Martin, F. Kaiser, M.P. De Micheli, O. Alibart, D.B. Ostrowsky. On the genesis and evolution of integrated quantum optics. Laser Photonics Rev. 6, 115–143 (2012).
25. B. J. Metcalf, J. B. Spring, P. C. Humphreys, N. Thomas-Peter, M. Barbieri, W. S. Kolthammer, X. M. Jin, N. K. Langford, D. Kundys, J. C. Gates, B. J. Smith, P. G. R. Smith, I. A. Walmsley, Quantum teleportation on a photonic chip. Nat. Photon. 8, 770–774 (2014).
26. A. Crespi, R. Ramponi, R. Osellame, L. Sansoni, I. Bongioanni, F. Sciarrino, G. Vallone, P. Mataloni. Integrated photonic quantum gates for polarization qubits. Nat. Commun. 2, 566 (2011).
27. J. Carolan, C. Harrold, C. Sparrow, E. Martín-López, N. J. Russell, J. W. Silverstone, P. J. Shadbolt, N. Matsuda, M. Oguma, M. Itoh, G. D. Marshall, M. G. Thompson, J. C. F. Matthews, T. Hashimoto, J. L. O'Brien, A. Laing. Universal linear optics. Science 349, 711-716(2015).
28. N. C. Harris, G. R. Steinbrecher, J. Mower, Y. Lahini, M. Prabhu, T. Jones, M. Hochberg, S. Lloyd, D. Englund. Bosonic transport simulations in a large scale programmable nanophotonic processor. arXiv:1507.03406 (2015).
29. W. H. P. Pernice, C. Schuck, O. Minaeva, M. Li, G. N. Goltsman, A. V. Sergienko, H. X. Tang. High-speed and high efficiency travelling wave single-photon detectors embedded in nanophotonic circuits. Nat. Commun. 3, 1325 (2012).
30. F. Najafi, J. Mower, N. C. Harris, F. Bellei, A. Dane, C. Lee, X. Hu, P. Kharel, F. Marsili, S. Assefa, K. K. Berggren, D. Englund, On-chip detection of non-classical light by scalable integration of single-photon detectors. Nat. Commun. 6 (2015).
31. N. C. Harris, D. Grassani, A. Simbula, M. Pant, M. Galli, T. B.-Jones, M. Hochberg, D. Englund, D. Bajoni, C. Galland, Integrated source of spectrally filtered correlated photons for large-scale quantum photonic systems. Phys. Rev. X 4, 041047 (2014).
32. T. Meany, L. A. Ngah, M. J. Collins, A. S. Clark, R. J. Williams, B. J. Eggleton, M. J. Steel, M. J. Withford, O. Alibart, S. Tanzilli, Hybrid photonic circuit for multiplexed heralded single photons. Laser Photonics Rev. 8, L42–L46 (2014).
33. G. Li, Recent advances in coherent optical communication, Advances in Optics and Photonics. 2, 279-307 (2009).
34. M. A. Nielsen, I. L. Chuang, Quantum Computation and Quantum Information. Cambridge University Press, 2004.
35. X. L. Wang, X. D. Cai, Z. E. Su, M. C. Chen, D. Wu, L. Li, N. L. Liu, C. Y. Lu, J. W. Pan, Quantum teleportation of multiple degrees of freedom of a single photon. Nature 518, 516–519 (2015).
36. V. D'Ambrosio, E. Nagali, S. P. Walborn, L. Aolita, S. Slussarenko, L. Marrucci, F. Sciarrino, Complete experimental toolbox for alignment-free quantum communication. Nat. Commun. 3, 961 (2012).
37. T. Inagaki, N. Matsuda, O. Tadanaga, M. Asobe, H. Takesue, Entanglement distribution over 300 km of fiber. Opt. Exp.,21, 23241–23249 (2013).
38. H. Hübel, M. R. Vanner, T. Lederer, B. Blauensteiner, T. Lorünser, A. Poppe, A. Zeilinger. High-fidelity transmission of polarization encoded qubits from an entangled source over 100 km of fiber. Opt. Exp., 15, 7853-7862 (2007).
39. N. Matsuda, H. Le Jeannic, H. Fukuda, T. Tsuchizawa, W. J. Munro, K. Shimizu, K. Yamada, Y. Tokura, H. Takesue, A monolithically integrated polarization entangled photon pair source on a silicon chip. Sci. Rep. 2, 817 (2012).
40. L. Olislager, J. Safioui, S. Clemmen, K. P. Huy, W. Bogaerts, R. Baets, P. Emplit, S. Massar, Silicon-on-insulator integrated source of polarization-entangled photons. Opt. Lett. 38, 1960–1962 (2013).
41. D. Taillaert, H. Chong, P. Borel, L. Frandsen, R. De La Rue, R. Baets, A compact two-dimensional grating coupler used as a polarization splitter. IEEE Photon. Technol. Lett. 15, 1249–1251 (2003).
42. D. Dai, J. E. Bowers, Silicon-based on-chip multiplexing technologies and devices for Peta-bit optical interconnects. Nanophotonics 3, 283–311 (2014).
43. X. Cai, J. Wang, M. J. Strain, B. Johnson-Morris, J. Zhu, M. Sorel, J. L. O'Brien, M. G. Thompson, S. Yu, Integrated compact optical vortex beam emitters. Science 338, 363–366 (2012).
44. D. Bonneau, E. Engin, K. Ohira, N. Suzuki, H. Yoshida, N. Iizuka, M. Ezaki, C. M. Natarajan, M. G. Tanner, R. H. Hadfield, S. N. Dorenbos, V. Zwiller, J. L. O'Brien, M. G. Thompson, Quantum interference and manipulation of entanglement in silicon wire waveguide quantum circuits. New J. Phys. 14, 045003 (2012).
45. S. Miki, T. Yamashita, H. Terai, Z. Wang, High performance fiber-coupled NbTiN superconducting nanowire single photon detectors with Gifford-McMahon cryocooler. Opt. Exp., 21, 10208-10214 (2013).
46. D. F. V. James, P. G. Kwiat, W. J. Munro, A. G. White. Measurement of qubits. Phy. Rev. A., 64, 052312 (2001).
47. W. Zaoui, A. Kunze, W. Vogel, M. Berroth, CMOS-Compatible Polarization Splitting Grating Couplers With a Backside Metal Mirror. IEEE Photon. Techn. Lett. 25, 1395-1397(2013).
48. L. B. Verslegers, A. Mekis, T. Pinguet, Y. Chi, G. Masini, P. Sun, A. Ayazi, K. Y. Hon, S. Sahni, S. Gloeckner, C. Baudot, F. Boeuf, and P. De Dobbelaere, "Design of Low-Loss Polarization Splitting Grating Couplers," in Advanced Photonics for Communications, OSA Technical Digest (online) (Optical Society of America, 2014), paper JT4A.2.
49. P. G. Kwiat, K. Mattle, H. Weinfurter, A. Zeilinger, A. V. Sergienko, Y. Shih, New high-intensity source of polarization entangled photon pairs. Phys. Rev. Lett. 75, 4337 (1995).
50. J. G. Rarity, P. R. Tapster, Experimental violation of bell's inequality based on phase and momentum. Phys. Rev. Lett. 64, 2495–2498 (1990).
51. J. F. Clauser, M. A. Horne, A. Shimony, R. A. Holt, Proposed experiment to test local hidden-variable theories. Phys. Rev. Lett. 23, 880–884 (1969).
52. K. Bartkiewicz, B. Horst, K. Lemr, A. Miranowicz, Entanglement estimation from Bell inequality violation. Phys. Rev. A 88, 052105 (2013).
53. Weihs, G., Jennewein, T., Simon, C., Weinfurter, H. & Zeilinger, A. Violation of Bell's inequality under strict Einstein locality conditions. Phys. Rev. Lett. 81, 5039–5043 (1998).
54. R. Fickler, R. Lapkiewicz, M. Huber, M. P. J. Lavery, M. J. Padgett, A. Zeilinger, Interface between path and OAM entanglement for high-dimensional photonic quantum information. Nat. Commun. 5, 4502 (2014).
55. M. J. Strain, X. Cai, J. Wang, J. Zhu, D. B. Phillips, L. Chen, M. Lopez-Garcia, J. L. O'Brien, M. G. Thompson, M. Sorel, S. Yu, Fast electrical switching of orbital angular momentum modes using ultra-compact integrated vortex emitters. Nat. Commun. 5, 4856 (2014).
56. C. Xiong, X. Zhang, A. Mahendra, J. He, D.-Y. Choi, C. J. Chae, D. Marpaung, A. Leinse, R. G. Heideman, M. Hoekman, C. G. H. Roeloffzen, R. M. Oldenbeuving, P. W. L. van Dijk, C. Taddei, P. H. W. Leong, B. J. Eggleton, Compact and reconfigurable silicon nitride time-bin entanglement circuit. Optica 2, 724–727 (2015).
57. D. Grassani, S. Azzini, M. Liscidini, M. Galli, M. J. Strain, M. Sorel, J. E. Sipe, D. Bajoni, Micrometer-scale integrated silicon source of time-energy entangled photons. Optica 2, 88-94 (2015).
58. J. Sun, E. Timurdogan, A. Yaacobi, E. S. Hosseini, M. R. Watts, Large-scale nanophotonic phased array. Nature 493, 195–199 (2013).
59. S. Han, T. J. Seok, N. Quack, B.-W. Yoo, M. C. Wu. Large-scale silicon photonic switches with movable directional couplers. Optica 2, 370–375(2015).
60. W. Bogaerts, R. Baets, P. Dumon, V. Wiaux, S. Beckx, D. Taillaert, B. Luyssaert, J. Van Campenhout, P. Bienstman, D. Van Thourhout, Nanophotonic waveguides in silicon-on-insulator fabricated with CMOS technology. Journal of Lightwave Technology 23, 401–412 (2005).